17th Brazilian Congress of Thermal Sciences and Engineering
November 25th-28th, 2018, Águas de Lindóia, SP, Brazil

ENCIT-2018-0452
A NUMERICAL STUDY OF THE CAPSULE-INTAKE FLOW OF A SCALED ELETRIC SUBMERSIBLE PUMP ON THE SKID (ESP-S)

Guilherme Alonso Solano
guilherme.alonso@ufabc.edu.br
Federal University of ABC, Santo André/SP 09210-580, São Paulo, Brazil

André Damiani Rocha
a.damiani@ufabc.edu.br
Federal University of ABC, Santo André/SP 09210-580, São Paulo, Brazil

Daniel Jonas Dezan
daniel.dezan@ufabc.edu.br
Federal University of ABC, Santo André/SP 09210-580, São Paulo, Brazil

Valdir Estevam
valdir_e@hotmail.com
University of Campinas

Antonio C. Bannwart
bannwart@fem.unicamp.br
University of Campinas

Abstract. *In the petroleum industry, artificial lift methods are responsible for raising the fluid to the surface when the energy from the reservoir is not enough for the production or can be used to increase the production flow of the well, resulting in gain in productivity. In this paper, the single-phase fluid flow characteristics in the capsule-intake of a scaled model of Electric Submersible Pump on the Skid (ESP-S) were investigated by means numerical approach. The steady state and unsteady numerical analysis have been carried out using Fluent® for turbulent Reynolds numbers equals to 80,249 in horizontal position. Pressure drop, axial and radial velocities components were computed. The pressure numerical results are compared with the experimental results. The components of velocity at intake's position showed that a secondary flow occurs in this specific region.*

Keywords: *ESP-S, Artificial Lift, CFD*

1. INTRODUCTION

In the petroleum industry, artificial lift methods are responsible for raising the fluid to the surface when the energy from the reservoir is not enough for the production or can be used to increase the production flow of the well, resulting in gain in productivity. Electric Submersible Pump (ESP) is one of the main artificial lift methods used in oil production. Flatern (2015) estimates that the system is installed in approximately 200,000 wells around the world. The components of the system are an electric motor, a motor protector, a pump that consists in multiple centrifugal stages and a power cable (Fig. 1.a). Each stage of the pump has a diffuser and an impeller, respectively the rotation component and the stationary component (Fig. 1.b).

The ESP-S (Electric Submersible Pump on the Skid) is a variation of the ESP model. The major difference between these pumping devices is the time required to perform an intervention on the equipment. Unlike the ESP, which is housed inside the well, the ESP-S is located on the seafloor. An ESP-S consists in two ESPs in the approximately horizontal position inside a caged-type module (Fig. 2). The two pumps are hydraulically connected in series and powered in parallel by a single umbilical power (Tarcha *et al*., 2015).

Some studies present the advantages of the ESP in the skid application when compared with other arrangements of ESP's (Roberto, et al., 2013; Tarcha, et al., 2015). Roberto, et al., 2013 presented the tests results of an ESP-S prototype at Atalaia's test site and real field tests.

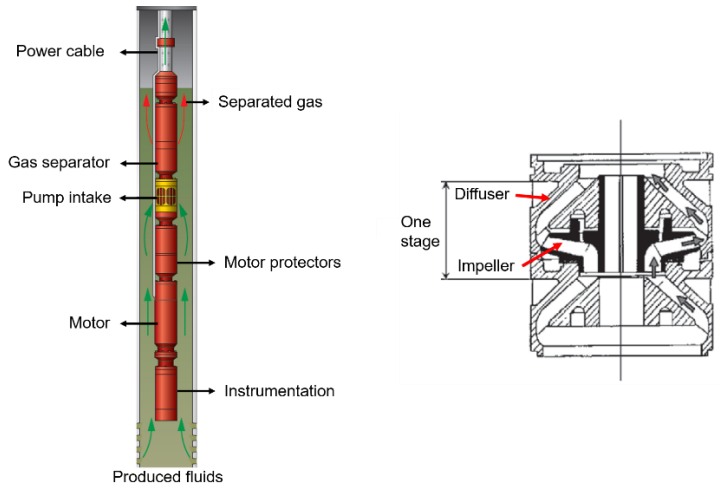

Figure 1. (a) Representation of the ESP. (b) One stage of a centrifugal pump (a. Flatern, 2015; b. Takács, 2009).

Homstved, *et al*., 2015 performed a comparative study between a jumper installed ESP, an ESP in a pump module (MOBO) and an ESP-S, emphasizing the benefits of modularity, installation/substitution easiness, operability and the customer's value. Tarcha, *et al*., 2015 presented the main developments of the ESP-S concept and conclude that this technology is a candidate to be applied where the fluid elevation is realized by pumping, them concluded also that it has installation advantages and lower maintenance costs.

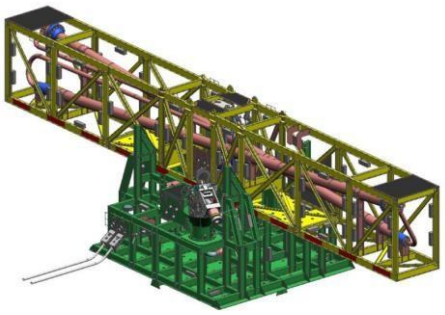

Figure 2. Representation of the ESP-S (Tarcha *et al*., 2015)

Tosta (2010) developed a two-phase flow study of water and gas in a MOBO installation using computational fluid dynamics techniques and the results were compared with the experimental results obtained at CENPES/Petrobras. The numerical model represented very well the experimental results, moreover, the authors also concluded that the geometric aspects of the equipment and the two-phase flow inside MOBO are contributing factors for the phases establishment.

ESP-S studies with the aim of characterizing the flow in the pump intake were not found in the literature. The capsule/intake region is dominated by secondary flow and recirculation zones that can influence the phases behavior defining the gas portion that enters through the intake and the portion that remain at the capsule annular. The gas portion that remains in the capsule intake can become a problem if it blocks the pumping, as it accumulates and reaches the intake region. Moreover, the flow is turbulent, representing a greater challenge in the phenomenon modeling.

In the literature it is possible to find results obtained with the Reynolds Average Navier-Stokes (RANS) methodology, the turbulence models were investigated to understand if they can approach with good agreement the problem. When compared to other methodologies, such as Large-Eddy Simulation (LES) and Direct Numeric Simulation (DNS), the RANS approach has a lower computational cost, which is a good advantage.

Thereby, the main aim of the present study is to characterize the flow in the capsule/intake region. The approach considered in this article was the single-phase turbulent flow using Fluent® for Reynolds number of 80,249, as in literature it was not possible to find any references about this subject. The model is a scaled model of the real experiment and it does not have the diffuser-impeller. The numerical results are compared with the experimental results realized at University of Campinas (UNICAMP), at the Petroleum Laboratory.

Problem Statement

Figure 3 shows the configurations and scale dimensions considered in this work. Upon entering the ESP-S system the fluid flows through the inlet tubing and then through the annular in the capsule, part of this fluid enters through the intake (with 6 orifices) and part goes through the annular. The capsule end is closed, and the fluid continues to flow only through the inner tube. No diffuser or impeller is considered here. The location of the pressure measurements collected in the experiment were also located in Fig. 3.

2. METHODOLOGY

The present work is developed through a numerical approach, using computational fluid dynamics techniques. The study of the grid independence was performed using the GCI (Grid Convergence Index) method, which ensures that the mesh is refined enough. Moreover, the axial velocity in three regions (inlet, annular and outlet) were compared with the analytical values and the pressure measurements collected by the experimental study were also compared with the numerical results. With the aim of choosing the turbulence RANS model, turbulence models used in studies that have a similar geometry were considered. Concentric pipes flows, with annular section, show similarity with the present study (Torii and Yang, 1994; Neto, *et al*., 2011). In addition, a validation study was conducted using the experimental results from the literature (Nouri, 1993) for a concentric annular duct.

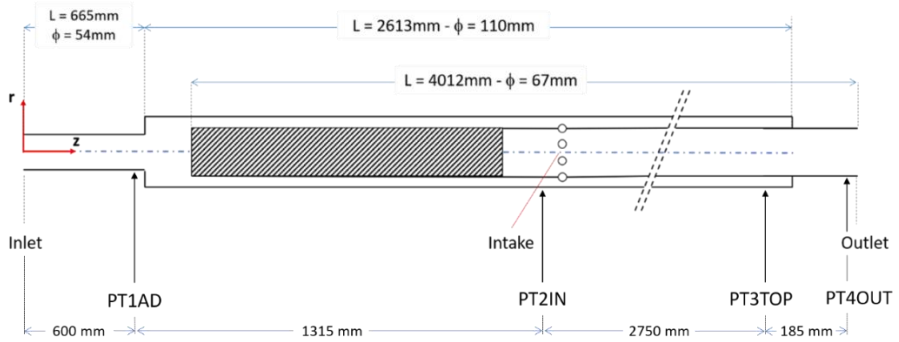

Figure 3. Computational domain.

Governing equations

Considering an unsteady, isothermal, incompressible and turbulent flow using the unsteady RANS (URANS) approach, the flow modelling was described by the continuity, momentum, turbulence kinetic energy (k) and specific dissipation rate (ω) as shown in Eq. 1, Eq. 2, Eq. 3 and Eq. 4, respectively. The RANS steady state equations are basically the same as the URANS equations, however, it does not consider the time-dependent term of the URANS equations.

$$\frac{\partial}{\partial x_j}(\rho u_i) = 0 \tag{1}$$

$$\frac{\partial}{\partial t}(\rho u_i) + \frac{\partial}{\partial x_j}(\rho u_i u_j) = -\frac{\partial p}{\partial x_i} + \frac{\partial}{\partial x_j}\left[\mu\left(\frac{\partial u_i}{\partial x_j} + \frac{\partial u_j}{\partial x_i}\right)\right] + \frac{\partial}{\partial x_j}\left(-\rho\overline{u_i' u_j'}\right) \tag{2}$$

where $i, j = 1,2,3$, x is the special coordinate, u mean velocity components, $\overline{u_i' u_j'}$ is the Reynolds stress components, u' denotes the fluctuating part of the velocity; p is the pressure, t is the time and ρ is the density of the fluid.

The $k-\omega$ SST model (Menter, 1994) is used at the present study, it is a variation of Wilcox (1998) $k-\omega$ Standard model. The $k-\omega$ SST model is a combination of the $k-\omega$ Standard model, which is good to approach a flow with near wall problems, and the $k-\varepsilon$ model, which is good to capture the turbulence effects far from the wall (free-stream).

$$\frac{\partial}{\partial t}(\rho k) + \frac{\partial}{\partial x_i}(\rho k u_i) = \frac{\partial}{\partial x_j}\left[\left(\mu + \frac{\mu_t}{\sigma_k}\right)\frac{\partial k}{\partial x_j}\right] + \widetilde{G_k} - \rho\beta^* k\omega \tag{3}$$

$$\frac{\partial}{\partial t}(\rho\omega) + \frac{\partial}{\partial x_j}(\rho\omega u_j) = \frac{\partial}{\partial x_j}\left[\left(\mu + \frac{\mu_t}{\sigma_\omega}\right)\frac{\partial \omega}{\partial x_j}\right] + G_\omega - \rho\beta\omega^2 + 2(1-F_1)\rho\frac{1}{\omega\sigma_{\omega,2}}\frac{\partial k}{\partial x_j}\frac{\partial \omega}{\partial x_j} \tag{4}$$

where the production of turbulence kinetic energy $(\widetilde{G_k})$ and production of ω (G_ω) are, respectively

$$\widetilde{G_k} = min(-\rho\overline{u_i' u_j'}\frac{\partial u_j}{\partial x_i}, 10\rho\beta^* k\omega) \tag{5}$$

$$G_\omega = \frac{\rho\alpha}{\mu_t}\widetilde{G_k} \tag{6}$$

The turbulent eddy viscosity is defined as

$$\mu_t = \frac{\rho k}{\omega}\frac{1}{\max\left[\frac{1}{\alpha^*}, \frac{SF_2}{a_1\omega}\right]} \tag{7}$$

The functions F_1 and F_2 are blending functions. F_1 is equal to zero away from the surface ($k-\varepsilon$ model) and switches over to one inside the boundary layer ($k-\omega$ SST). S is the invariant measure of strain rate. The constants of $k-\omega$ SST model are: $\beta^* = 0{,}09$, $\sigma_{\omega,2} = 1.168$, $\alpha = 1$, $\alpha^* = 1$, $a_1 = 0.31$. Further information on the model can be found in (Fluent, 2018).

The presence of a wall has a large influence of the flow behavior and structure of a turbulent flow. Far from the wall the inertial forces dominating and close to the wall the flow is influenced by viscous effects and does not depend of the free stream parameters. For the fluid adjacent to the wall, the relationship between velocity and distance from the wall is linear and this is only valid for an extremely thin layer (viscous sub-layer) or normal dimensionless distance to the wall less than 5 ($y^+ < 5$). It is well accepted that this value for $k-\omega$ SST model should be close to unity. For all cases of this paper the value of y^+ was less than 1.

The numerical analysis has been carried out using Fluent®. The Semi-Implicit Method for Pressure Linked Equations (SIMPLE) was used for the pressure-velocity coupling. The second order upwind discretization scheme was used for pressure and convection terms. The computational convergence criteria are ensured, making the residuals lower than $1x10^{-5}$ and the time step was $1x10^{-4}$.

Some important parameters like mean velocity equation (Eq. 8), mean pressure equation (Eq. 9) and Reynolds number equation (Eq. 10) are described as

$$\bar{V} = \frac{\int_A V\, dA}{\int_A dA} \tag{8}$$

$$\bar{p} = \frac{\int_A p\, dA}{\int_A dA} \tag{9}$$

$$Re = \frac{\rho\bar{V}D}{\mu} \tag{10}$$

where $\bar{V}$ the mean velocity, $\bar{p}$ the mean pressure and A the transversal section area.

Boundary conditions

The boundary conditions used for the simulation are set as follows: the mass flow rate ($\dot{W}$) is set at the inlet boundary. Moreover, the turbulence intensity (I_T) and the hydraulic diameter (D_h) are calculated as follows:

$$I_T = 0{,}16Re^{-1/8} \tag{11}$$

$$D_h = D_e \tag{12}$$

where the Reynolds number and hydraulic diameter are based on the inlet pipe diameter.

At outlet boundary the pressure is specified. The turbulence intensity and the hydraulic diameter are calculated using the same definitions as Eq. 11 and Eq. 12, however, it is based on the outlet pipe diameter. A no-slip boundary condition is prescribed in all domain walls.

3. GRID INDEPENDECE STUDY

The grid independence study was carried on using the Grid Convergence Index (GCI) proposed by Roache (1994). Three different grids and the variation of the total pressure gradient ($\Delta p = \bar{p}_{outlet} - \bar{p}_{inlet}$) were used to verify the independence of the results with the grid. For all cases, the y^+ was lower than 1. The grid test was realized in steady state for Reynolds number equals to 80,249. The flow conditions are presented in Tab. 1.

Table 1. Boundary conditions for the GCI studies.

$\dot{W}_{inlet}$	Re	$I_{T-inlet}$	$I_{T-outlet}$	P_{outlet}
[kg/s]	[-]	[%]	[%]	[Pa]
9.316	80,249	3.344	3.435	170,171

The GCI method requires a variable and the cells grid number, the results of the GCI method are in Tab. 2. As the GCI method uses the Richardson extrapolation to evaluate if the numerical results converge to an asymptotic result, Fig. 4 shows this comparison between the numerical results and the Richardson extrapolation.

Table 2. Grid independence analysis for the present work.

Grid	Cell Number	Δp	GCI
[-]	[-]	[Pa]	[%]
Coarse	14,940,869	25,981.52	-
Medium	17,111,290	25,639.91	3.487
Refined	23,669,393	25,205.75	1.394

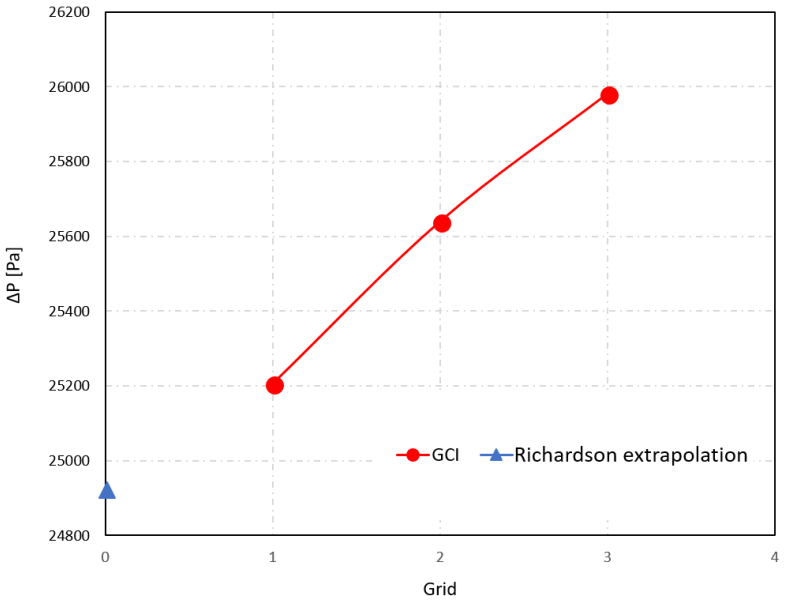

Figure 4. Comparison between the numerical results and the Richardson extrapolation.

The GCI study resulted in the validation of the grid as the asymptotic behavior was observed in Fig. 4 and the GCI value was around 1.4%. So, as the relative error related to the refined grid was low (1.4%), in the main study the refined grid was used with approximately 23.7 million cells.

4. RESULTS/DISCUSSION

Before performing the simulations of the present study, turbulent steady state flow simulations were performed in a concentric annular section tube to validate the computational model and the turbulence models considered were: $k-\omega$ SST and Reynolds Stress Model (RSM; Launder *et al.*, 1975; Gibson and Launder, 1978; Launder, 1989). The validation study was performed using the experimental results of Nouri *et al.* (1993). Figure 5 shows the axial velocity distribution weighted by flow average velocity as a function of the annular gap (r/S), the error bars considered in this case is equal to 5.5%. Considering the computational costs between the two models and the approximation of both results, the $k-\omega$ SST model was chosen to be used in the principal simulation.

Varying the flow-time from $0\ s$ to 1.25 second, due computational cost, some variables were computed to understand the flow in the intake region. Velocity and pressure through time were collected in the pump intake

region, velocities profiles were computed, and other analysis were carried out. Also, the steady state simulation was considered so it can be compared with the unsteady simulation results.

4.1 Steady state and unsteady comparison

The numerical mean axial velocity and the mean pressure were obtained in a specific surface that is a transversal section of the pipe exactly at the pump intake location, approximately at $2.04\ m$ from the inlet. Figure 6(a) represents the mean axial velocity distribution in that specific area through time, as observed before the simulation flow-time was 1.25 second. Figure 6(b) shows the mean pressure through time.

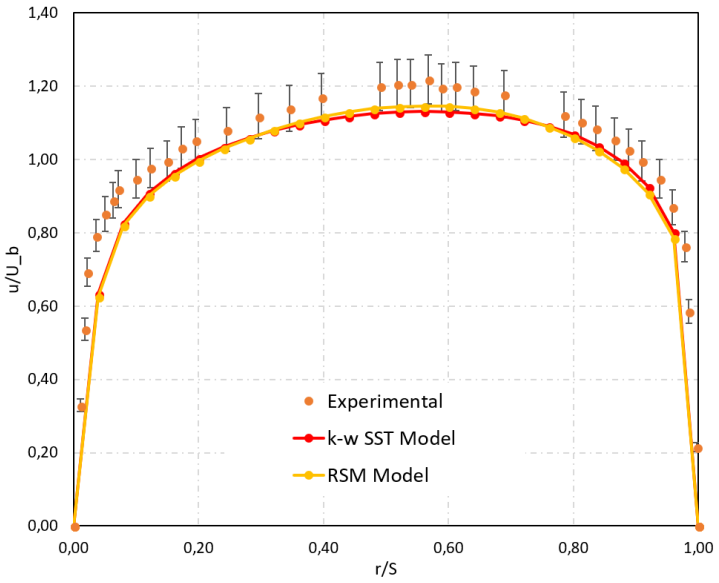

Figure 5. Simulated and experimental results for axial velocity profiles normalized with bulk velocity.

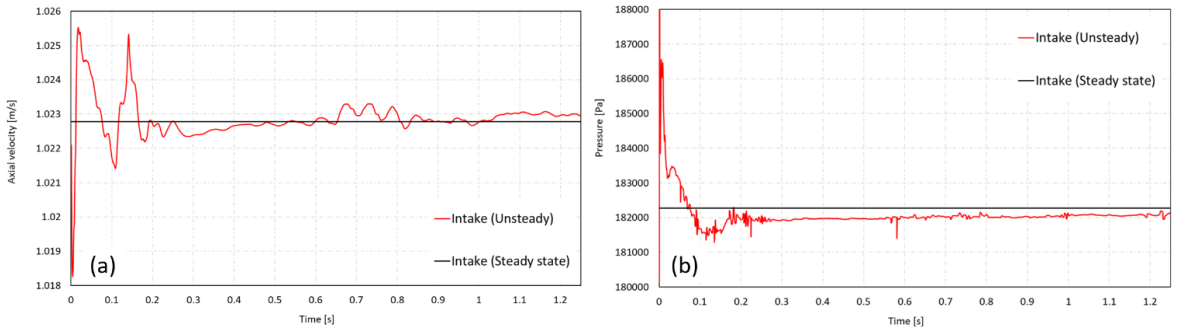

Figure 6. Velocity and Pressure: (a) Mean axial velocity through time;
(b) mean pressure through time – intake region.

For the velocity comparison it is possible to analyze a convergence behavior of the unsteady results, where until the time limit of 1.25 second the unsteady results tends to converge to the steady state numerical result. Similarly, the mean pressure results also seem to converge to the steady state result.

4.2 Pressure - Experimental versus Numerical Results

The measured pressures were compared with the numerical values of the steady state solution so it was possible to calculate the relative error (Eq. 13) between them.

$$E = \left| \frac{\emptyset_{exp,calc} - \emptyset_{num}}{\emptyset_{exp,calc}} \right| . 100 \qquad (13)$$

where $\emptyset$ in pressure analysis is pressure (experimental value) and in velocity analysis is the mean velocity (calculated value).

Four pressure measurements were collected in the experiment and then compared with the numerical results at the same position as shown in Fig. 3. This comparison is displayed in Tab. 3 and the maximum relative error is around 2.5%, showing that the numerical results agree very well with the experimental results.

Table 3. Error analysis for pressure.

		PT1AD	PT2IN	PT3TOP	PT4OUT
P_{exp}	[Pa]	191,840.87	193,524.95	189,137.33	170,171.45
P_{num}	[Pa]	193,417.64	188,714.52	189,569.54	170,048.44
E	[%]	0.82	2.49	0.23	0.07

4.3 Flow Field Analysis

The mean axial velocity values for the numerical simulation (Eq. 8) also agree very well with the analytical values (V_a), where the maximum relative error is around 1% as shown in Tab. 4. These analytical results were calculated from the mass flow rate and the continuity equation.

Table 4. Error analysis for the mean axial velocity.

		V_{inlet}	$V_{annular}$	V_{outlet}
V_a	[m/s]	4.085	1.84	2.654
V_{num}	[m/s]	4.119	1.839	2.6543
E	[%]	0.85	0.01	-0.01

The velocity components and magnitude distribution were collected over a line as shown in Fig. 7, the line length is 1 m and it is located at the capsule annular demonstrated in the isometric surface and in the transversal section surface. Figure 7(a) is the steady state results and Fig. 7(b) is the unsteady results for 1.25 second. Both results show that the Radial velocity only exists at the intake location outside that region it is zero and its maximum value appears at the center of the intake's orifice direction, represent by the dashed line, around 2.04 m having a value of $-1.5\ m/s$ representing that the flow is in the negative direction of r.

The axial velocity remains constant from 1.6 m to approximately 2 m having a value of 2 m/s. Approaching at the intake's orifice it decays below zero indicating a region of opposite flow, negative direction of z, both for the steady state and the unsteady solutions. However, Fig. 7(a) shows that the axial velocity decays below zero and then becomes positive again at approximately 2.1 m, this behavior suggests a recirculation region as will be discussed later. The axial velocity for the unsteady solution decays more than the steady state solution and it does not reach a positive velocity after the peak of approximately 1.2 m/s, emphasizing that the flow is in the negative direction of z as will be demonstrated in section 4.4. Another behavior that highlights the difference between the steady state and the unsteady results is that the velocities reach zero at different positions. In Fig. 7(a) the annular capsule flow stops at 2.4 m, on the other hand, in Fig. 7(b) it stops at approximately 2.25 m.

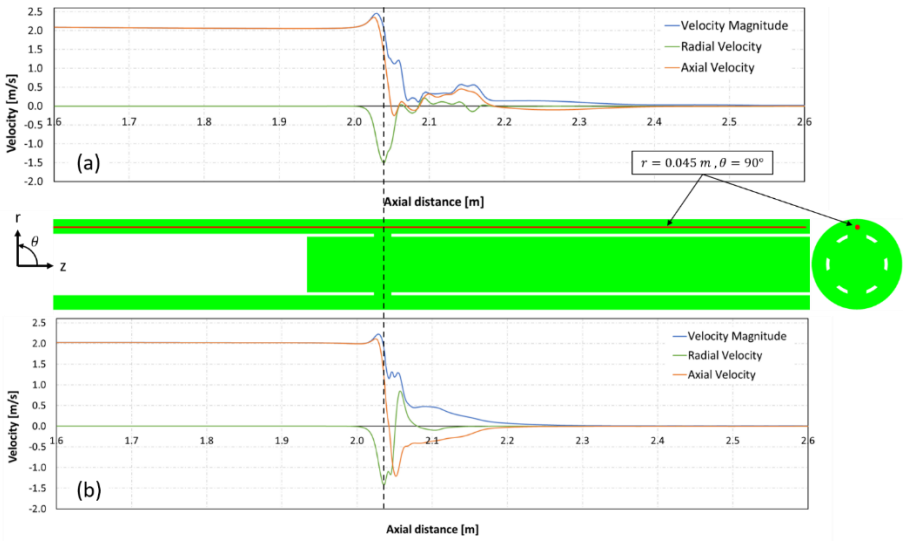

Figure 7. Velocity components and magnitude – (a) steady state; (b) unsteady for $t = 1.25\ s$.

Figure 8 is the axial velocity profile collected in a line located at the center of the intake, as also shown in Fig. 8, for different time-steps and for the steady state solution. The inner pipe wall is represented by the dashed line. As the no-slip condition was considered at walls, for $r = 0.055\ m$ and $-0.055\ m$, which is the pipe radius, the axial velocity is zero for all cases. For all solutions the axial velocity increases as it approaches the intake orifice due to the flow and the area restriction imposed in this region. Analyzing the flow symmetry, it seems to be asymmetric until $t = 1.2\ s$ because the axial velocity behavior from $r = 0\ m$ to $0.055\ m$ is different from $r = 0\ m$ to $-0.055\ m$. The axial velocity at the center of the pipe turns to the negative direction of z.

For $t = 0.9\ s$ the behavior of the axial velocity at the center of the pipe differs from the other time-steps and even from the steady state solution. The maximum value of the parameter at that time-step is approximately $-2.5\ m/s$ and its location is $r = 0.005\ m$. Moreover, near the top of the outer pipe wall the velocity reaches a higher value compared from the bottom of the outer pipe wall. When time reaches $1\ s$ it is possible to observe kind of a symmetric flow and it is reinforced at $1.2\ s$.

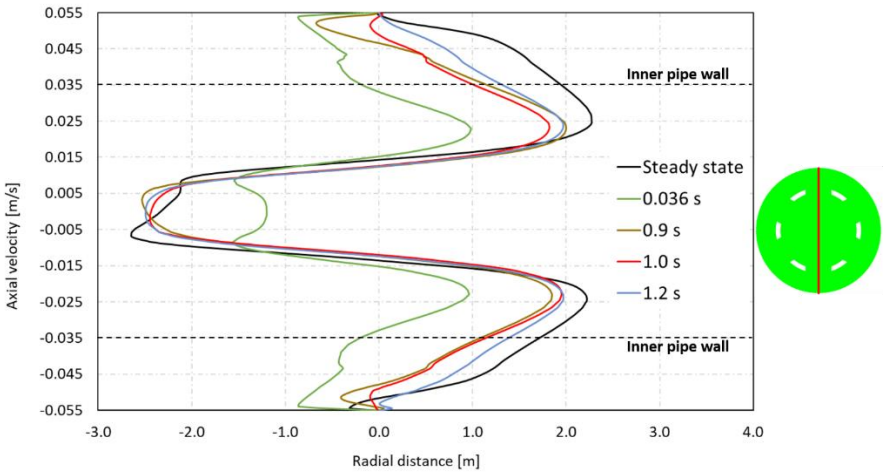

Figure 8. Axial velocity profile at the intake ($z = 2.04\ m$).

The axial and radial velocity profile were collected at the same flow-time, which is $1.25\ s$. Figure 9 shows the axial velocity profile at the capsule/intake region. As shown in Fig. 9 the characteristic of the axial velocity profile appears after intake region, where the maximum value of axial velocity is in the center of the tube, which is $6.31\ m/s$, far from the wall where the velocity is zero due to the no-slip condition. Negative velocities can be seen in some zones indicating that the flow direction at that specific zone is in the opposite direction to the principal flow direction, which is towards the outlet or positive z coordinate.

Radial velocity profiles were collected at the same region as shown in Fig 10. Note that the radial velocity appears only in the intake region, as discussed before at Fig. 7(b) analyses. The negative velocities in Fig. 10 indicates that the flow direction is the center of the tube. The maximum absolute value of the radial velocity appears in the center of the intake orifice, also discussed before in Fig. 7(b).

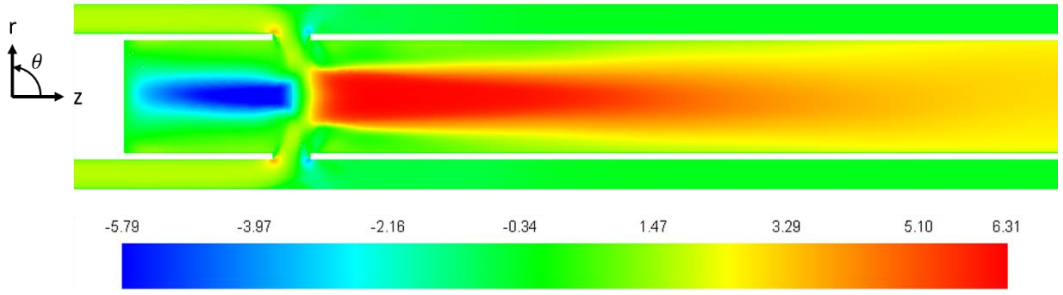

Figure 9. Axial velocity profile for $t = 1.25\ s$ – capsule/intake region.

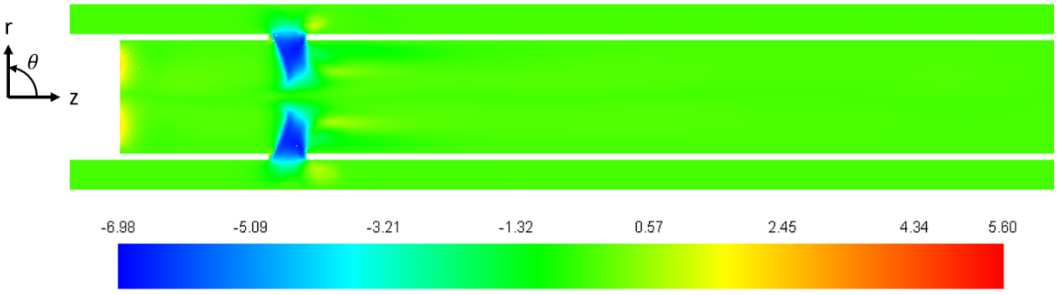

Figure 10. Radial velocity profile for $t = 1.25\ s$ – capsule/intake region.

4.4 Recirculation zones and reversed flow

As discussed in section 4.3, there are some regions the flow seems to return. To investigate this behavior Fig. 11(a) and Fig. 11(b) present the magnitude velocity streamline for the steady state solution and for $t = 1.25\ s$,

respectively. The streamlines were collected to analyze these recirculation zones present in the study. Focusing on Fig. 11(a) there are some recirculation activity both in the annular capsule and in the inner pipe, but highlighting the top of the annular capsule, where in Fig. 7(a) there was a suspicion of a recirculation region based on the axial velocity, here it visually appears. As discussed before in Fig. 8, after $1.2\ s$ the flow presents a more symmetric behavior, and this can be seen in Fig. 11(b) where in the inner pipe the streamline seems to be similar both above and below the center of the pipe, it cannot be considered a symmetric flow because at the annular capsule the top flow differs from the bottom and also there is a limit of time-step in this study of $1.25\ s$.

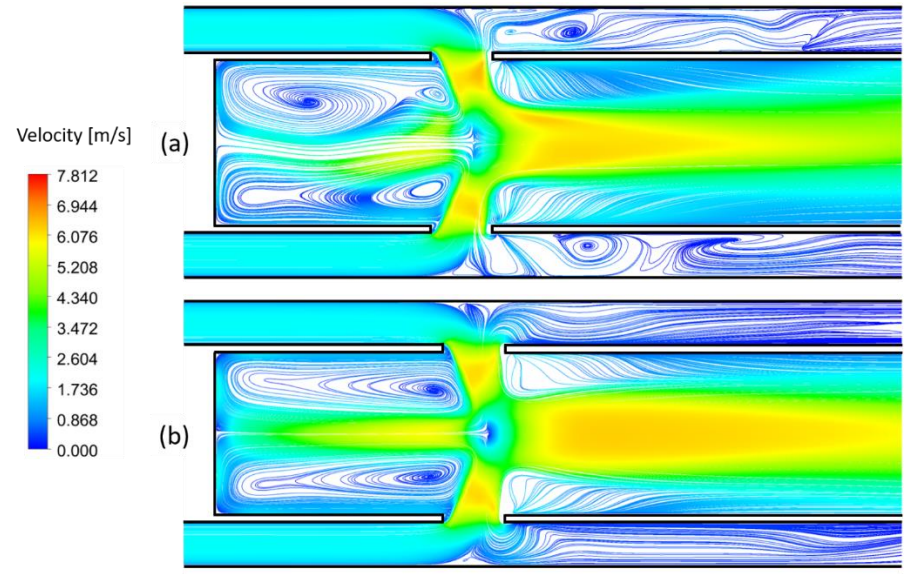

Figure 11. Streamline at the intake region – (a) steady state; (b) unsteady for $t = 1.25\ s$.

Immediately after the intake region, the flow becomes a reversed flow, where the flow takes the opposite direction. Figure 12 represents the velocity magnitude vectors focusing on the intake, more precisely at the top orifice for $t = 1.25\ s$. The dashed line represents the centerline of the pipe. The capsule annular velocity before the intake presents a developed profile, as expected. Note that when the flow gets closer to the intake it turns to a radial direction. The flow after the orifice is reversed in nearby locations and it seems to decrease or even stop as it moves away from the intake.

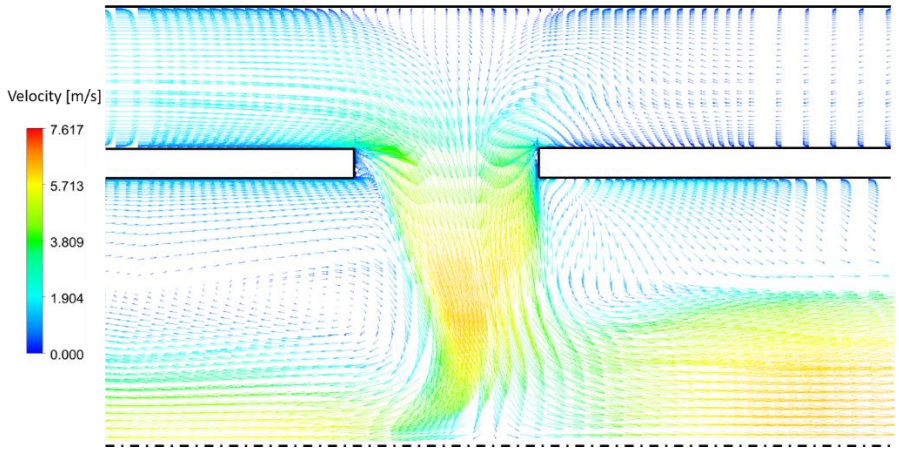

Figure 12. Velocity magnitude vectors at the intake region.

Other view of the intake is the transversal section shown in Fig. 13. The figures 13(a) and 13(b) represents the magnitude velocity for the steady state solution and for $t = 1.25\ s$. Similarly, to a flow through an orifice plate presented by Tukiman (2017), at the intake's orifices two recirculation zones appear for each of the six orifices. The unsteady differs from the steady state solution in some points like in the center of the pipe and other streamlines that are distorted in steady state solution.

5. CONCLUSION

In this work, a numerical study was carried out with the purpose of simulate the capsule-intake flow of an ESP-S. The intake region of the equipment has an important role to the flow as the results showed that the velocity field

is totally changed by this region. It was also observed that some recirculation and reversed flow zones are present along the domain.

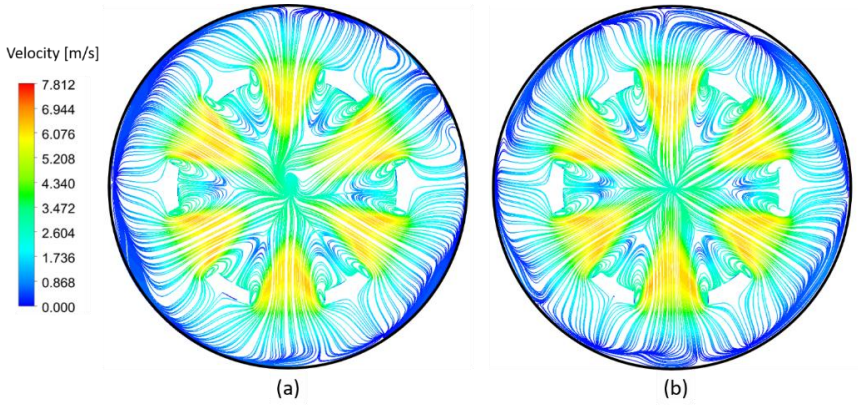

Figure 13. Streamline at the intake surface ($z = 2.04\ m$) – (a) steady state; (b) unsteady for $t = 1.25\ s$.

The numerical results obtained by the steady state and unsteady numerical simulation, for Reynolds number equals to $80{,}249$, were compared with the experimental results and showed good agreement.

The flow field was analyzed and although the radial velocity component did not predominate in the capsule annular region, in intake it is a crucial parameter where the main flow changes the direction, disarranging it. The capsule after intake is a region of stagnation, where the fluid stops and accumulates in the end.

Finally, the unsteady numerical study showed the secondary flow region downstream and upstream at intake's position.

6. ACKNOWLEDGEMENTS

The authors thank Petrobras and ANP for providing financial support for this work. Acknowledgments are also extended to ALFA – Artificial Lift & Flow Assurance Research Group.

7. REFERENCES

Fluent; "Theory Guide", ANSYS Inc., USA (2018).

Flatern, R. V.; "The Defining Series - Electrical Submersible Pumps", Oilfield Review, 2015.

Gibson, M. M.; Launder, B. E., "Ground Effects on Pressure Fluctuations in the Atmospheric Boundary Layer", J. Fluid Mechanics, 86, p. 491-511, 1978.

Homstvedt, G; Pessoa, R.; Portman, L.; Wang, S.; Gonzalez, J.; Maldaner, M.; Margulis, J.; "Step-Change Seabed ESP Boosting", Offshore Technology Conference, 2015.

Launder, B. E., "Second-Moment Closure: Pressure and Future?", Int. J. Heat and Fluid Flow, 10, p. 282-300, 1989.

Launder, B. E.; Reece, G. J.; Rodi, W., 'Progress in the Development of a Reynolds-Stress Turbulence Closure", J. Fluid Mechanics, 68, p. 537-566, 1975.

Menter, F. R.; "Two-Equation Eddy-Viscosity Turbulence Models for Engineering Applications", AIAA Journal, vol. 32, No. 8, p. 1598-1605, 1994.

Nouri, J. M.; Umur, H.; Whitelaw, J. H.; "Flow of Newtonian and non-Newtonian Fluids in Concentric and Eccentric Annuli", Journal of Fluid Mechanics, vol. 253, p. 617-641, 1993.

Roache, P. J.; "Perspective: a Method for Uniform Reporting of Grid Refinement Studies", Journal of Fluids Engineering, vol. 116, p. 405-413, 1994.

Roberto, M. A. R.; Oliveira, P. S.; Pyramo, B. M.; "Mudline ESP: Electrical Submersible Pump Installed in a Subsea Skid", Offshore Technology Conference, 2013.

Tarcha, B. A.; Borges, O. C.; Furtado, R. G.; "ESP Installed in a Subsea Skid at Jubarte Field", SPE Artificial Lift Conference, p. 27-28, 2015.

Torii, S.; Yang, W. J.; "Numerical Study on Turbulent Flow and Heat Transfer in Circular Couette Flows", Numerical Heat Transfer, Part A, 26, p. 321-336, 1994.

Tosta da Silva, L. C.; "Simulação Numérica de Poço Alojador de Bombeio", Universidade Federal do Rio de Janeiro, 2010.

Tukiman, M. M.; Ghazali, M. N. M.; Sadikin, A.; Nasir, N. F.; Nordin, N.; Sapit, A.; Razali, M. A.; "CFD Simulation of Flow Through an Orifice Plate", IOP Conference Series: Materials Science and Engineering, 2017.

Vieira Neto, J. L.; Martins, A. L.; Silveira Neto, A.; Ataíde, C. H.; Barrozo, M. A. S.; "CFD Applied to Turbulent Flows in Concentric and Eccentric Annuli with Inner Shaft Rotation", The Canadian Journal of Chemical Engineering, vol. 89, p. 636-646, 2011.

Wilcox, D. C.; "Turbulence Modeling for CFD", DCW Industries, Inc., 1993.